Electrochimica Acta 374 (2021) 137968

Contents lists available at ScienceDirect

Electrochimica Acta

journal homepage: www.elsevier.com/locate/electacta

Mechanistic insights of the oxidation of bisphenol A at ultrasonication assisted polyaniline-Au nanoparticles composite for highly sensitive electrochemical sensor

Md. Mahedi Hasan[a,1], Tamanna Islam[a,1], Al Imran[a], Bassam Alqahtani[b], Syed Shaheen Shah[c], Wael Mahfoz[d], Mohammad Rezaul Karim[e,f], Hamad F. Alharbi[b], Md. Abdul Aziz[c,*], A.J. Saleh Ahammad[a,*]

[a] Department of Chemistry, Jagannath University, Dhaka 1100, Bangladesh
[b] Department of Mechanical Engineering, College of Engineering, King Saud University, Riyadh 11421 Saudi Arabia
[c] Center of Research Excellence in Nanotechnology, King Fahd University of Petroleum & Minerals, Dhahran 31261, Saudi Arabia
[d] Chemistry Department, King Fahd University of Petroleum & Minerals, Dhahran 31261, Saudi Arabia
[e] Center of Excellence for Research in Engineering Materials, Deanship of Scientific Research (DSR), King Saud University, Riyadh 11421, Saudi Arabia
[f] K.A.CARE Energy Research and Innovation Center, Riyadh 11451, Saudi Arabia

ARTICLE INFO

Article history:
Received 13 August 2020
Revised 23 December 2020
Accepted 9 February 2021
Available online 12 February 2021

Keywords:
Bisphenol A
Ultrasonication
Polyaniline
Gold nanoparticles
Electrocatalysts

ABSTRACT

In this work, a conducting polymer and nanometal composite electrocatalyst was prepared for the sensitive detection of bisphenol A (BPA) over a wide concentration window. Polyaniline (PANI) was first prepared from aniline through a chemical method, and gold nanoparticles (AuNPs) were embedded with the prepared PANI via ultrasonication to obtain the PANI_AuNPs electrocatalyst. The morphological, chemical, and electrochemical properties of the electrocatalyst were then determined, and BPA oxidation was investigated with the help of electroanalytical techniques to understand the electron-transfer process occurring at the PANI_AuNPs interface. The results showed that BPA was oxidized through a multistep electron-transfer process without any intermediate chemical step, and the rate-determining step was the second electron-transfer step. The oxidation proceeded as a $2e^-/2H^+$ process with an electron-transfer coefficient of ≈0.69. These results indicate that the PANI and AuNPs work synergistically to promote the electron transfer from BPA. The quantitative analysis gave a broad linear range and a low limit of detection of 0.4 nM. The sensor was also tested for the detection of BPA in tap water, bottled water, and a canned beverage for real sample analysis.

1. Introduction

Bisphenol A (BPA) is a key ingredient of polycarbonate plastics (PCPs) and epoxy resins [1,2]. In these PCPs, the BPA monomer is reacted with phosgene to form esters, while alkylation is used for epoxy resin production [3–5]. These PCPs are often used for manufacturing clear water bottles, baby bottles, and sports equipment products [6,7]. The epoxy resins are used in coatings for food containers, water pipes, and sales paper products [7,8]. More than a million tons of BPA are used per year for these purposes [8,9]. Products containing BPA are usually stable, robust, and do not leach [9]. However, upon heating, the polymers can degrade and cause BPA leaching into water, baby food, or other products [10]. As an endocrine disruptor, BPA can simulate or block hormones related to endogenic activities and cause serious harm to both animals and humans [8,11]. Excessive BPA in the body has been associated with cancer, degradation of sperm quality, thyroid problems, and even diabetes [6,12]. Since 2015, the European Food Safety Authority has set the daily tolerable BPA consumption level to 0.4 μg kg^{-1} [13]. Therefore, a sensitive, selective, and accurate detection system that can provide instant results is necessary. Commonly used techniques such as chromatography, spectroscopy, and fluorescence are highly sensitive and can give accurate results, but they often require tedious sample preparation, expensive instruments, and expert operators [8,11,14]. An alternative to these techniques is electrochemical sensors (ECSs), which are accurate,

* Corresponding authors.
E-mail addresses: maziz@kfupm.edu.sa (Md.A. Aziz), ajsahammad@chem.jnu.ac.bd (A.J.S. Ahammad).
[1] These authors contributed equally to this work.

https://doi.org/10.1016/j.electacta.2021.137968
0013-4686/

sensitive, quick, inexpensive, and simple means to detect environmental pollutants and biomolecules [13–16].

Base electrodes (e.g., indium tin oxide, glassy carbon (GC), fluorine-doped tin oxide) often need to be modified with conducting polymers and/or nanomaterials for preparing effective electrochemical BPA sensors [17–20]. However, most of the modified electrodes are either very sensitive with a narrow linear range or have a wide linear range with low sensitivity [17,19,21]. Some composite modifiers have been reported that simultaneously show a wide linear range and good sensitivity for BPA detection. For instance, Poorahong et al. reported polyaniline (PANI) rods with multi-walled carbon nanotubes (MWCNTs) over a graphite pencil electrode for BPA detection over a wide linear range [8]. PANI has also been used with ruthenium nanoparticles (RuNPs) and graphene oxide (GO) for BPA sensing [17,18]. The PANI-RuNPs composite showed a linear range from 10 nM to 1.1 μM with a sensitivity of 1.6 μA cm^{-2} μM^{-1}, while the PANI-GO composite demonstrated a broad linear range from 2 nM to 3 μM and a low LOD of 0.5 nM [17, 18]. Niu et al. reported that graphene nanoribbon (GPN) with gold nanoparticles (AuNPs) over a GC electrode (GCE) can detect BPA with good sensitivity over a broad linear range [11]. In another work, AuNPs were incorporated with polyvinylpyrrolidone (PVP) through an electrochemical method over graphite electrode for sensitive detection of BPA [12]. The AuNPs/PVP-modified electrode showed an impressive linear range from 23 nM to 1.1 μM with an LOD of 1 nM [12]. Hence, composite electrocatalysts prepared with conducting polymers and metal nanoparticles might provide an effective route for sensitive BPA detection with a broad linear range.

In order to prepare active electrocatalysts for BPA detection, it is important to understand the catalytic activity of the electrode modifiers towards the analyte [22,23]. To understand the catalytic process, it is essential to investigate the kinetics of BPA oxidation at the modifier material [24]. Combining the kinetics of the electron-transfer process with the materials characterization data can give good insight into the electrochemical reaction mechanism. This way, the contribution of modifiers towards the electron-transfer process can be evaluated, and this knowledge can be used to prepare electrocatalysts with refined properties [25].

In this work, we chose to incorporate PANI and AuNPs into our composite modifier for BPA detection because previous reports for both materials have shown that they can detect BPA with high sensitivity over a wide linear range. We then determined the morphological and chemical properties of the PANI_AuNPs composite along with the kinetics of the electron-transfer process at the PANI_AuNPs interface during BPA oxidation. Based on the obtained results, a possible BPA oxidation reaction mechanism is proposed. To test its performance in real-life scenarios, the prepared ECS was used for quantitative detection of BPA in water samples and canned beverage.

2. Materials and methods

2.1. Chemicals and materials

BPA [$(CH_3)_2C(C_6H_4OH)_2$], gold(III) chloride hydrate [$HAuCl_4$], L-ascorbic acid, potassium persulfate, monobasic and dibasic sodium phosphate, catechol (CT), sodium carbonate, magnesium carbonate, potassium nitrate, and hydroquinone (HQ) were all purchased from Sigma-Aldrich, Germany. Aniline and ethanol were obtained from BDH Chemicals Ltd. and Honeywell, respectively. For electrochemical experiments, all analytes were tested in solutions containing 0.1 M phosphate buffer (PB), unless stated otherwise. Deionized water was used for standard tests. For real sample analysis, the sources were tap water, bottled water, and canned beverage.

2.2. Instrumentation

A CHI 660E potentiostat (CH Instruments, USA) was used in all electrochemical experiments. A three-electrode system with working (GCE, PANI_GCE, or PANI_AuNPs/GCE), counter (Pt wire), and reference (Ag/AgCl, 3 M) electrodes was used. X-ray diffraction (XRD) spectra were recorded on a Rigaku MiniFlex-II X-ray diffractometer (Rigaku, Japan) using $CuK_{\alpha 1}$ radiation (γ = 0.15416 nm); the tube current was 10 mA at an accelerating voltage of 30 kV. Field emission scanning electron microscopy (FESEM; Lyra3, Tescan, Czech Republic) with a 20 kV accelerating voltage was used for the morphological analysis. The FESEM instrument was equipped with an Oxford Instruments X-mass detector for measuring the energy dispersive X-ray spectrum (EDS). X-ray photoelectron spectroscopy (XPS) was measured on an ESCALAB 250Xi XPS Microprobe, (Thermo Scientific, USA). A Powersonic 603 Ultrasonic Cleaner (Kleentek, Australia) was used to clean the polished electrodes and disperse the modifier materials in the solvent.

2.3. Preparation of polyaniline (PANI) through chemical method

We prepared the PANI material according to a previously published method with slight modification [26]. Initially, we prepared solutions of monomer (aniline) and initiator (potassium persulfate ($K_2S_2O_8$)) (we used potassium persulfate instead of ammonium persulfate because it is more environmentally friendly). Then, these two solutions were mixed in a specific molar ratio of 1:1.25 (monomer: initiator) to initiate the synthesis process. The monomer solution was prepared in 1.0 M HCl (50 mL) by dissolving 0.5 ml of aniline. The initiator solution was also prepared in 1.0 M HCl (50 ml). For this purpose, 1.55 g of potassium persulfate was used. After mixing the monomer and initiator solutions, they were stirred for 20 min. At the final stage of polymerization, 100 ml of distilled water was added to finish the polymerization. The precipitated mass was washed with 1.0 M HCl and ethanol after filtration. The washed and filtered PANI was then dried for 30 min at 60 °C. Scheme 1A shows the synthesis process of PANI.

2.4. Synthesis of PANI_AuNPs electrocatalyst and preparation of PANI_AuNPs/GCE

To prepare the PANI_AuNPs composite, PANI (6 mg) was dispersed in distilled water (6 mL) by ultrasonication. In this dispersed mixture, 10 mM $HAuCl_4$ (3 mL) was added with manual shaking. In the final step, 20 mM ascorbic acid (3 mL) was added as a stabilizing agent to this mixture under ultrasonication, and the mixture was sonicated for 5 min to obtain the PANI_AuNPs composite. The synthesis scheme is shown in Scheme 1B.

The PANI_AuNPs/GCE was prepared through a simple drop-casting method in which PANI_AuNPs (2 mg) was first dispersed in a 3 mL solution of ethanol (1.5 mL) and water (1.5 mL). The mixture was sonicated for 30 min to disperse the PANI_AuNPs in the solution. Then, approximately 4 μL of the dispersed solution was drop casted on the polished GCE. The modified electrode was then dried at room temperature (RT). PANI/GCE was prepared using the same procedure. The PANI_AuNPs/GCE fabrication process is shown in Scheme 1C.

2.5. Method for determining the BPA oxidation mechanism at the PANI_AuNPs/GCE interface

To determine the reaction mechanism of BPA oxidation at the PANI_AuNPs/GCE interface, we considered the chemical and morphological properties of the PANI_AuNPs composite and the reaction kinetics of BPA oxidation. FESEM was used for evaluating the surface morphology, and EDS and XPS were used to determine the

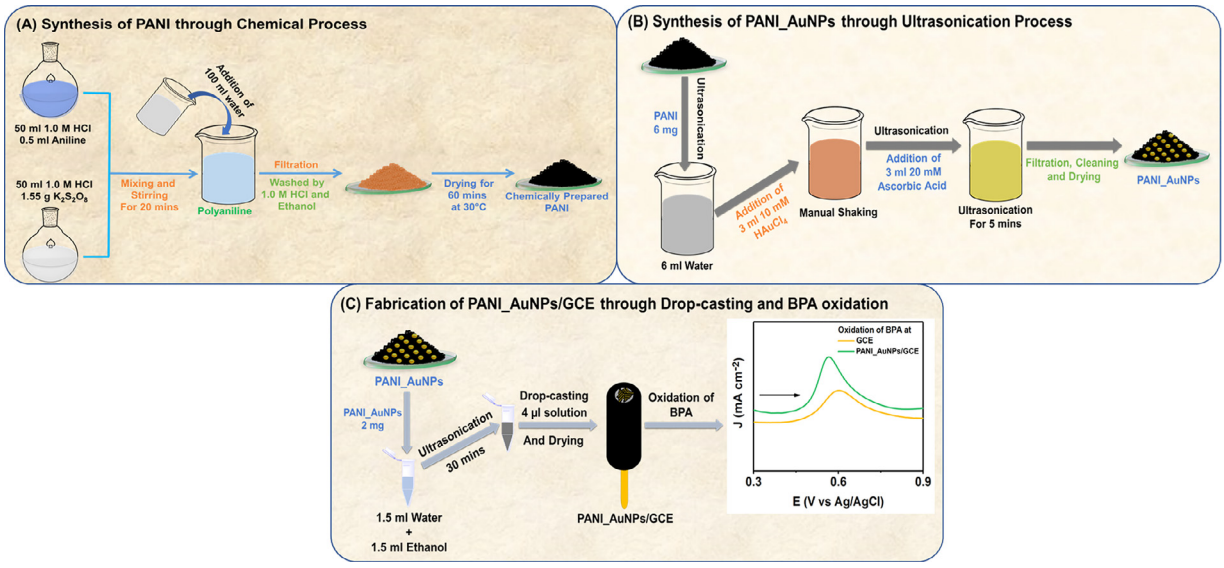

Scheme 1. Synthesis of PANI, PANI_AuNPs composite, and fabrication of PANI_AuNPs/GCE. A) Synthesis of PANI from aniline using a chemical method. B) Preparation of PANI_AuNPs using an ultrasonication process. C) Fabrication of PANI_AuNPs/GCE and its application towards BPA oxidation.

elemental composition and functional groups present. Afterward, XRD spectra were obtained to analyze the crystalline features of the PANI_AuNPs material, and its electrochemical properties were analyzed with the help of cyclic voltammetry (CV). The results of these studies elucidated the various chemical, morphological, and electrical properties of the PANI_AuNPs composite.

The kinetics of BPA oxidation at the PANI_AuNPs/GCE interface were then studied. Scan rate analysis was performed to determine whether the reaction process was controlled by diffusion or adsorption. We also determined the irreversibility of the BPA oxidation at the PANI_AuNPs/GCE from scan rate analysis. The number of electron transfer (n), electroactive surface area (A), heterogenous electron transfer rate constant (k), and electron transfer coefficient (α) for BPA oxidation at the PANI_AuNPs interface were determined using the equations for irreversible electron-transfer process derived from the Butler–Volmer (BV) equation. We subsequently used a Tafel plot to analyze the rate-determining step of the multielectron-transfer process. We also studied the kinetics of BPA oxidation at the PANI/GCE interface for comparison with the PANI_AuNPs/GCE system. The effect of pH and the proton to electron (m/n) transfer ratio was analyzed by varying the pH of the supporting electrolyte solution during BPA oxidation with the help of the Nernst equation.

Finally, after analyzing all the data, we proposed a mechanism of BPA oxidation at the PANI_AuNPs/GCE interface.

2.6. Method for evaluating the applicability of PANI_AuNPs/GCE as BPA sensor

To test the application of the PANI_AuNPs/GCE as a potential BPA sensor, we performed a quantitative analysis of BPA oxidation over a broad concentration window with the help of differential pulse voltammetry (DPV). From the obtained DPV plots, we measured the peak current values and plotted them against concentration. This plot allowed us to determine the linear range, sensitivity, and limit of detection (LOD) for BPA oxidation at the PANI_AuNPs/GCE interface.

Afterwards, we evaluated the selectivity of the PANI_AuNPs/GCE sensor through an interference test. Some of the most common environmental pollutants that undergo oxidation around the oxidation potential of BPA were tested [17]. We also employed DPV for testing the selectivity.

Both the experimental and storage stability of the PANI_AuNPs/GCE sensors were tested as well as the reproducibility of the sensor by modifying four different electrodes with PANI_AuNPs.

Finally, we tested the performance of the PANI_AuNPs/GCE sensor in tap water, bottled water, and canned beverage. The samples were prepared using the procedure described in the literature [13,17].

3. Results and discussion

3.1. Characterization of the PANI_AuNPs

Fig. 1 shows the FESEM, TEM, and EDS analyses of the PANI and AuNPs incorporated into the polymer material through the ultrasonication method (PANI_AuNPs). Figure S1A and Fig. 1A show the low and high-magnification FESEM images of the PANI, indicating the presence of cylindrical-rod-shaped structures. The TEM images of PANI further confirm this analysis (Fig. 1B). On the other hand, the high-resolution TEM image of PANI does not show any spherical structures (Fig. 1C). However, FESEM reveals that spherical AuNPs with an average size of less than 10 nm were sparingly scattered over the polymer surface (Figure S1B and Fig. 1D). In the TEM images, the AuNPs appear to congregate over certain areas of the PANI (Fig. 1E). The exact cause of this is not clear to us; it could be due to the dilution of the PANI_AuNPs sample with ethanol before transferring it to the TEM grid. However, the magnified images (Figure S2A, B) reveal that the sizes of the AuNPs are in the range of 5 – 10 nm, which is similar to the SEM observations. At the same time, TEM further confirms our analysis of the PANI and PANI_AuNPs materials (Figure S3). The selected area electron diffraction (SAED) pattern of PANI_AuNPs (Figure S3D) shows clear rings for the (111), (200), (220), and (311) planes of AuNPs [27]. However, Figure S3B does not contain any such rings for PANI.

In order to properly analyze the impact of ultrasonication during PANI_AuNPs synthesis, we also prepared PANI_AuNPs by stirring only. The FESEM image for PANI_AuNPs(stir) is shown in Figure S4. Both the low- (Figure S4A) and high-magnification (Figure S4B) images show that AuNPs aggregated on the PANI structure. This confirms that such highly controlled synthetic formulation and orientation of AuNPs over the polymer resulted from successful ultrasonication. In addition, when AuNPs are in-

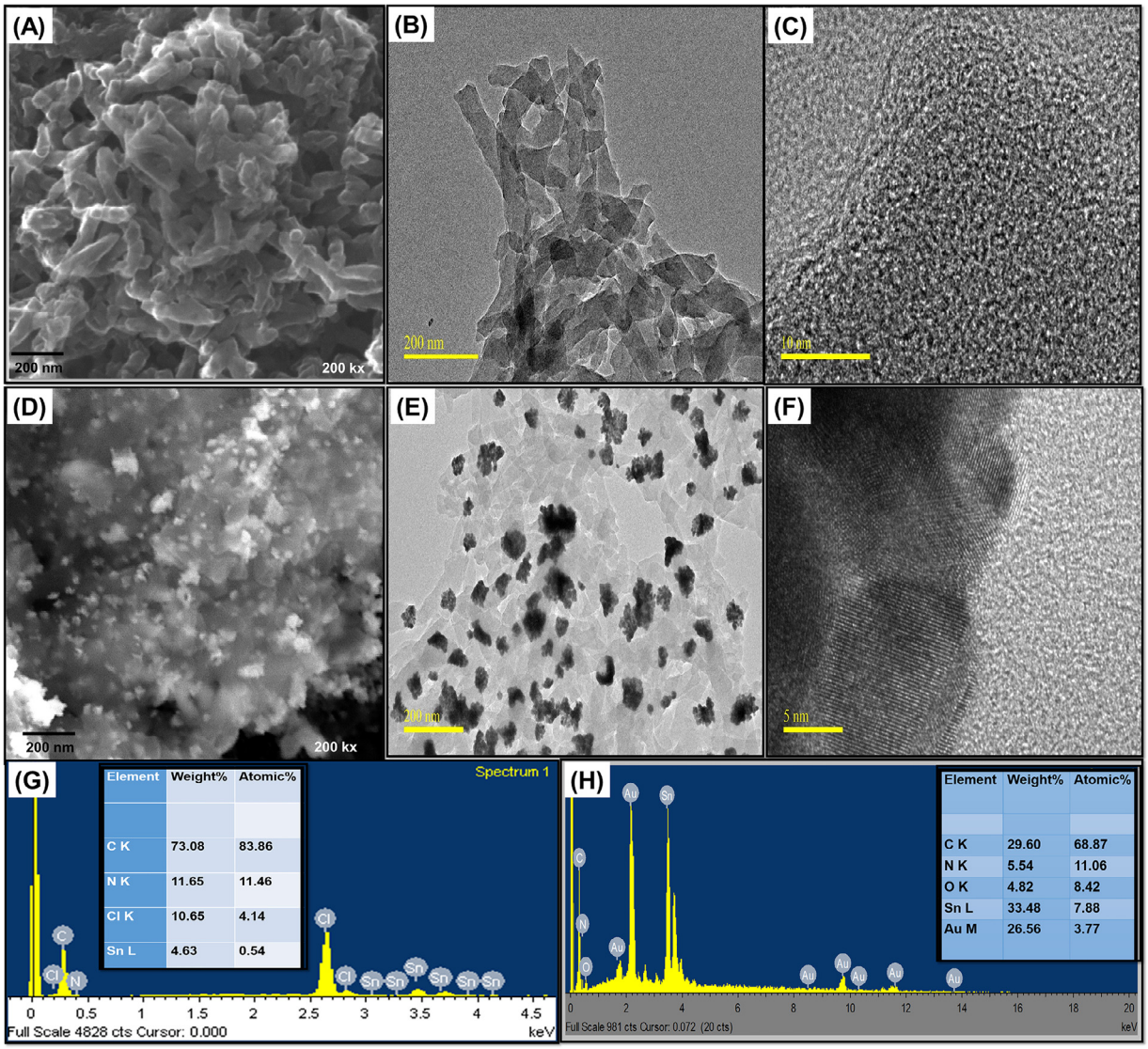

Fig. 1. Morphological analysis of PANI and PANI_AuNPs. FESEM (A) and TEM (B,C) images of PANI with different magnifications. FESEM (D) and TEM (E,F) images of PANI_AuNPs with different magnifications. EDS spectrum of (G) PANI and (H) PANI_AuNPs with a table showing the weight and atomic percentages of different elements.

corporated, it not only improves the conductivity of the overall electrode material but also provides a large effective surface for electrochemical interaction with the analyte necessary for initiating the low-energy electron-transfer process [28]. Figure S5 includes images of the PANI_AuNPs prepared through stirring and ultrasonication and shows a clear contrast between the two composite materials. EDS analysis revealed the elemental composition of PANI and PANI_AuNPs; PANI was comprised mainly of C (Fig. 1G), and PANI_AuNPs was comprised of 68.87% C, 11% N, 8.42% O, and 3.77% Au (Fig. 1H). The EDS also detected about 8% Sn, which can be attributed to the bare electrode surface remaining exposed in the direction of the light.

To further understand the variation in chemical composition, we conducted XPS analyses of both PANI and PANI_AuNPs (Fig. 2). The XPS survey scan of PANI in Fig. 2A reveals that the material mainly consisted of C, N, and O elements (core levels are indicated in the spectrum). Trace amounts of Cl and S were also present, which were likely due to the utilization of HCl and persulfate as the solvent and initiator, respectively, in the polymer synthesis. In contrast, the XPS survey scan of PANI_AuNPs showed two more core levels for Au (Au4d and Au4f) along with the other three for C, N, and O (Fig. 2B). This variation is proof that AuNPs were incorporated within the polymer via ultrasonication. We deconvoluted the XPS peaks of C1s, O1s, N1s, and Au4f core levels for PANI_AuNPs using the Gaussian fitting method. Fig. 2C shows the deconvoluted XPS C1s spectrum. The peak deconvolution resulted in two distinct peaks at 284.4 and 286 eV, which are attributed to C–C/C–H and C–O groups [29,30]. The O1s peak deconvolution resulted in two separate peaks due to spin-orbit splitting and are attributed to carboxylic acid (–COOH at 531.6 eV) and alcohol (–OH at 532.3 eV) groups (Fig. 2D) [29,30]. The N1s peak splits into two due to the deconvolution of the N1s core level. These two peaks can be assigned as pyramidal N–H (at 399.5 eV) and pyrrolic N (at 400.8 eV) groups, which are the essential structural features of PANI [31]. In the case of the Au4f core level, survey XPS showed two distinct peaks, namely $Au4f_{5/2}$ and $Au4f_{7/2}$, which appeared due to the initial spin-orbit scattering by X-ray [31]. The position of these peaks was around 84.3 and 88.0 eV. In addition, two more peaks were observed in the survey spectrum for the Au4d core level within 327–359 eV [31]. The percentages of the four core levels obtained from the XPS survey scan (C1s, O1s, N1s, and Au4f) were estimated to be approximately 79.25%, 8.98%, 9.3%, and 2.5%, respectively. Therefore, the XPS analysis of PANI_AuNPs demonstrates

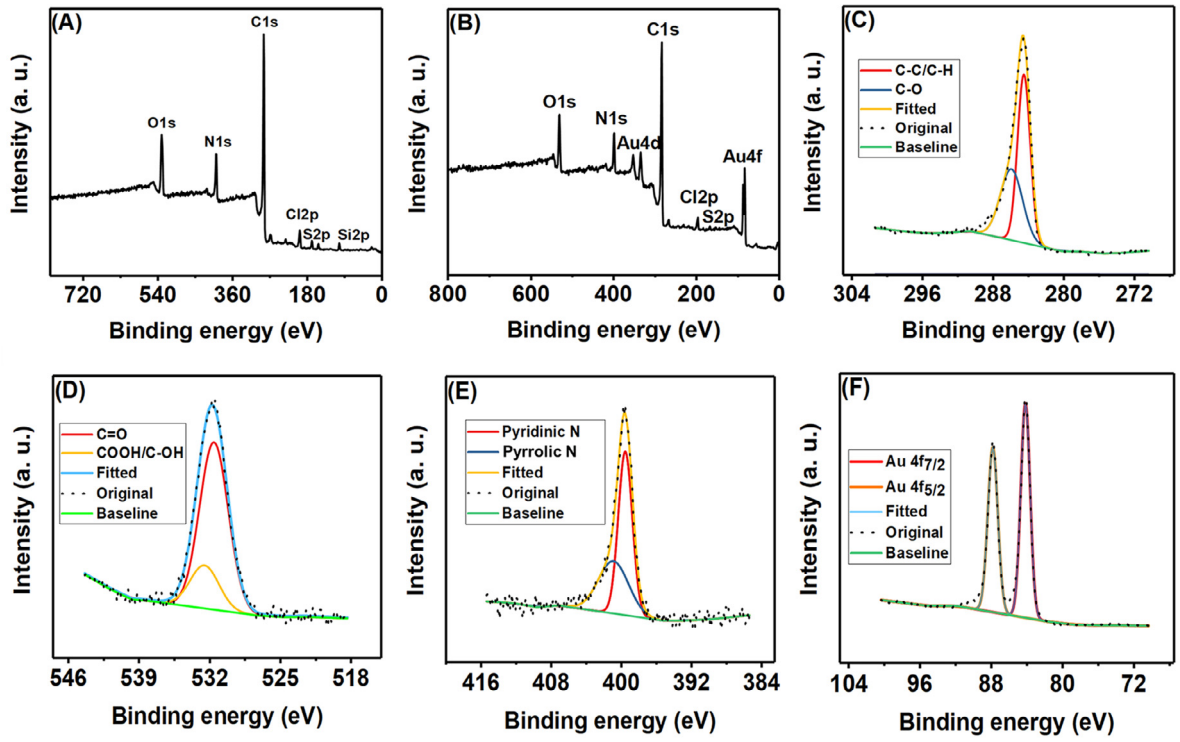

Fig. 2. XPS analysis of PANI and PANI_AuNPs. A, B) Survey spectra of PANI and PANI_AuNPs. C–F) Deconvoluted XPS spectra of C1s (C), O1s (D), N1s (E), and Au4f (F), respectively, for PANI_AuNPs.

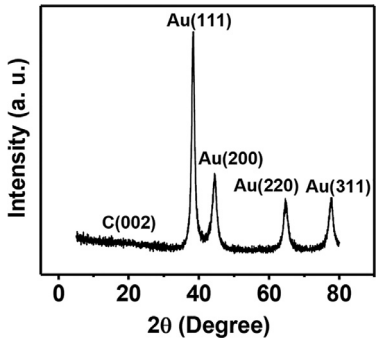

Fig. 3. XRD spectrum of PANI_AuNPs composite. Four sharp peaks are visible for the AuNPs and a broad shallow peak for carbon.

that PANI and AuNPs retain their properties in ultrasonically prepared PANI_AuNPs composite.

We further investigated the crystalline properties of the PANI_AuNPs composite by XRD analysis. Fig. 3 shows the XRD spectrum, which contains four consecutive intense peaks at 38.4°, 44.5°, 64.6°, and 77.7° corresponding to the (111), (200), (220), and (311) planes, respectively, of Au [32]. The crystallinity percentage of AuNPs in the composite was calculated to be 76.6% using the following equation.

$$Crystallinity = \frac{peak\ area\ under\ four\ planes}{total\ area\ (crystalline + amorphous)} \times\ 100\% \quad (1)$$

A slightly intense peak at around 22° appeared in the spectrum, which corresponds to graphitic crystallites and indicates that the polymer is partly graphitic in nature [28,30]. Figure S6 shows the XRD pattern for the PANI, in which the peak around 22° is clearly visible.

We investigated the electrochemical properties of the prepared PANI_AuNPs composite via ultrasonication in 0.1 M neutral phosphate-buffered saline (PBS) using CV. Fig. 4A shows the CV data obtained for polished GCE and GCE modified with PANI_AuNPs (PANI_AuNPs/GCE). It is clear from Fig. 4A that GCE did not exhibit an electron transfer response in the potential window of −0.2 to 1.0 V in the 0.1 M PBS. On the other hand, the PANI_AuNPs/GCE showed a well-defined redox signal around −0.1 to 0.1 V (denoted as (i)) and a small reduction response around 0.55 V (denoted as (ii)). The redox signal in (i) is most likely due to the oxidation of neutral PANI emeraldine form to a partially oxidized nigraniline and vice versa in the reduction sweep [33,34]. The current response around 0.55 V was due to the reduction of AuNPs present at the PANI_AuNPs composite [35]. The weak electron-transfer response of the AuNPs compared to the PANI is likely due to the fact that only a small amount of AuNPs was present on the PANI. The inset of Fig. 4A shows a magnified view of the reduction signal. This analysis confirms that the chemical treatment was successful in forming conducting PANI from aniline. Furthermore, AuNPs were incorporated within the PANI structure.

We studied the stability of the PANI_AuNPs composite through 25 consecutive CVs; Fig. 4B shows the overlay plot. After the second CV, the redox signal decreased only slightly, and the peak potential remained consistent throughout all the CVs. The peak current was retained by ≈97.91% ((7.96×10^{-6} A/ 8.13×10^{-6} A) × 100), and the relative standard deviation (RSD) for peak current response was calculated to be ≈2.60% for the consecutive CVs, confirming that the PANI_AuNPs remained attached to the surface of GCE and gave a stable response.

3.2. Oxidation of BPA at the PANI_AuNPs/GCE interface

We studied the oxidation of BPA at GCE and PANI_AuNPs/GCE using 0.1 M PBS and 50 μM BPA in 0.1 M PBS. We used CV and DPV techniques to investigate the oxidation of BPA at the PANI_AuNPs/GCE. Fig. 5A shows the CV responses for the bare and modified electrodes in blank and 50 μM BPA solutions. The GCE did

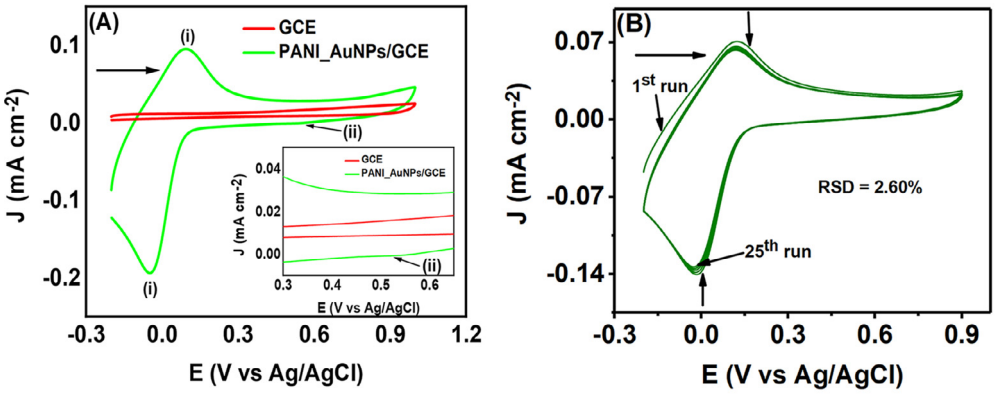

Fig. 4. Electrochemical characterization of PANI_AuNPs in 0.1 M PBS (pH 7.0). A) CV data from −0.2 to 1.0 V for GCE and PANI_AuNPs/GCE. Inset shows the magnified view for the potential window of 0.3 to 0.65 V. B) The change in peak current signal for 25 consecutive CVs in the PBS solution for determining the stability of the PANI_AuNPs/GCE.

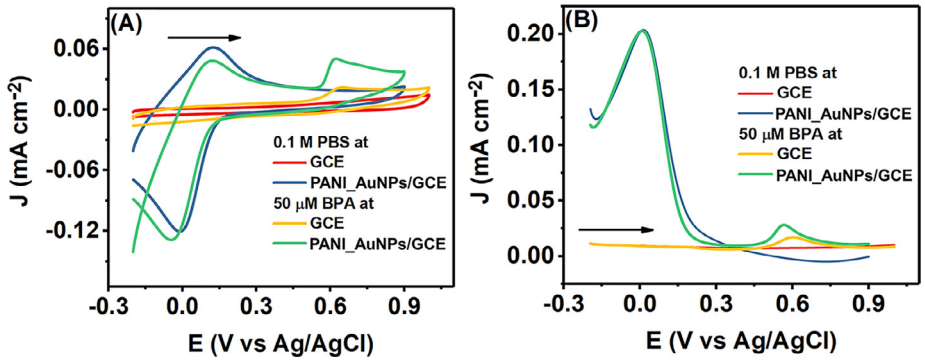

Fig. 5. Oxidation of BPA at polished GCE and PANI_AuNPs/GCE in 0.1 M neutral PBS. A) CVs taken at 50 mV s^{-1} with polished GCE and PANI_AuNPs/GCE in blank PBS solutions and 50 μM BPA solutions. B) DPVs taken with polished GCE and PANI_AuNPs/GCE in blank PBS solutions and 50 μM BPA solutions.

not show any response for the PBS but showed an oxidation signal at around ≈0.65 V for the BPA solution. The PANI_AuNPs/GCE showed the redox signals for PANI and AuNPs in the PBS and a signal around ≈0.62 V in the BPA solution. The peak current value for the oxidation of PANI_AuNPs/GCE (2.05×10^{-6} A) was almost ≈2.24 times higher than the GCE (9.17×10^{-7} A). We further investigated the BPA oxidation with DPV (Fig. 5B). Similar to the CV experiments, GCE and PANI_AuNPs/GCE did not give any current signal in the PBS around 0.6 V. In the BPA solution, GCE and PANI_AuNPs/GCE showed peak currents around ≈0.61 V and ≈0.56 V, respectively. The peak current ratio for PANI_AuNPs/GCE (1.27×10^{-6} A) and GCE (6.92×10^{-7} A) was ≈1.84. Both the CV and DPV analysis showed that the PANI_AuNPs/GCE is capable of oxidizing BPA at a lower potential with a much higher current value.

We also compared the performance of PANI_AuNPs/GCE with PANI/GCE for BPA oxidation. Figure S7A shows the CV data; PANI/GCE has a smaller peak current of 5.59×10^{-7} A at a lower positive potential of 0.61 V. The DPV response for PANI is shown in Figure S7B. PANI/GCE has a smaller oxidation current signal (2.76×10^{-7} A) in the DPV as well. These analyses confirm that the PANI_AuNPs composite has excellent electrocatalytic efficiency towards BPA oxidation compared to PANI.

3.3. Kinetics of BPA oxidation at the PANI_AuNPs/GCE interface

The effect of the scan rate on the voltammetric plot was evaluated to elucidate the kinetics of the heterogeneous electron-transfer process of the modified electrode towards BPA oxidation. Fig. 6A shows the increment of peak currents for BPA oxidation in eight different CV plots with scan rates increasing from 5 to 150 mV s^{-1}. The kinetics of BPA oxidation at the PANI/GCE interface was also investigated for comparison and that data is shown in Figure S8. The oxidation process was confirmed to be diffusion controlled for both systems after analyzing the calibration plot of oxidation peak current density vs. the square root of the scan rates. A plot of J_{pa} vs. $\nu^{1/2}$ is represented by a linear regression equation (Fig. 6B and Figure S8B). To confirm the irreversible nature of the electrochemical reaction, we further analyzed the relationship between the peak potential and the scan rates through an $I_p\ C^{-1}\ \nu^{-1/2}$ vs. log ν plot (Fig. 6C and Figure S8C). A plot of E_{pa} vs. log ν shows a linear relationship (Fig. 6D and Figure S8D). Therefore, for a typical irreversible reaction, the following equation is applicable:

$$E_p = Y + \frac{2.303RT}{2(1-\alpha)n_\alpha F}\log \nu \qquad (2)$$

Where R, T, and F represent the universal gas constant, temperature, and Faraday's constant, respectively; n_α denotes the number of electrons transferred in the rate-determining step (RDS); and α corresponds to the heterogeneous electron-transfer coefficient, which indicates whether the transition state relating to RDS is reactant- (<1) or product-like (close to 1). Using the slope of Eq. (2), we calculated the value of α corresponding to the BPA oxidation process at the PANI_AuNPs/GCE electrode as 0.69. For PANI/GCE, α was determined to be 0.75. These values demonstrate that the oxidation process is electrochemically feasible, and the electron transfer through the interfaces occurred by overcoming a comparatively low amount of activation energy over the modified electrode surface. The 0.75 value for PANI/GCE is consistent with the CV and DPV analysis that showed the BPA oxidation peak at a slightly more negative potential.

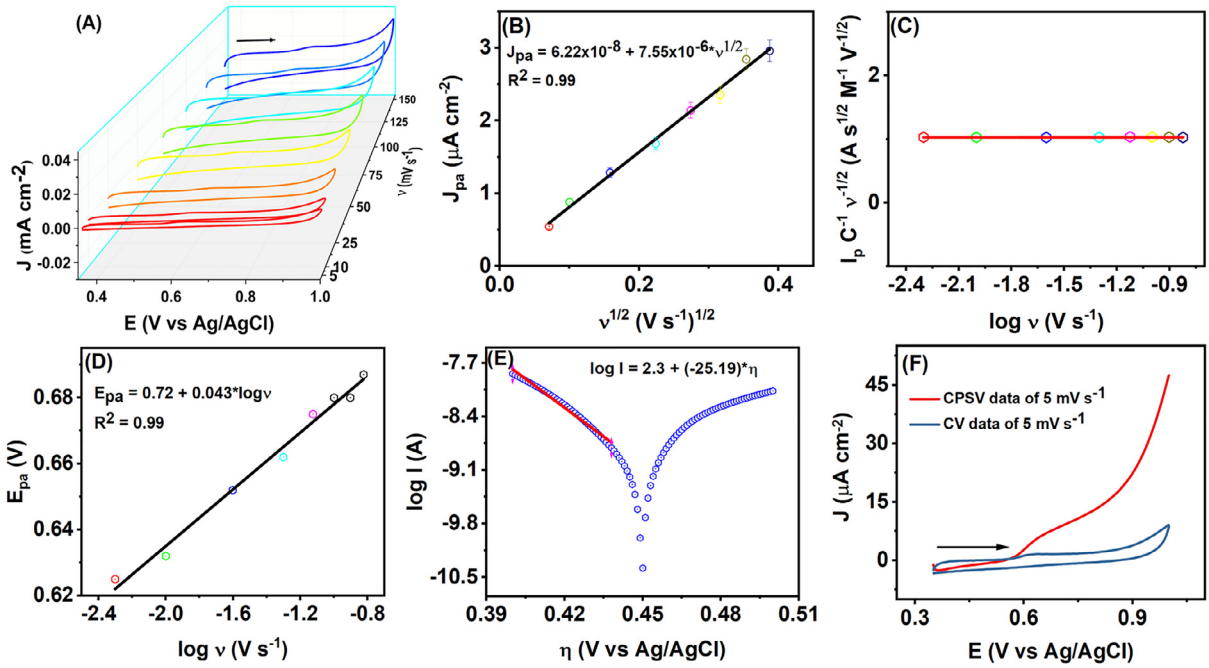

Fig. 6. Effect of scan rate on BPA oxidation at the PANI_AuNPs/GCE interface and analysis of the data for evaluating the electron transfer kinetics. Scan-rate variation experiments were carried out in a 0.5 μM BPA solution containing 0.1 M PBS (pH = 7.0). A) The following scan rates were used for the experiments: *a* – *h*) 5, 10, 25, 50, 75, 100, 125, and 150 mV s^{-1}. B) Peak current (J_{pa}) vs. square root of scan rate ($v^{1/2}$) plot. C) I_p C^{-1} $v^{-1/2}$ vs. log *v* plot. D) Peak potential (E_{pa}) vs. log *v* plot *v*. E) Tafel plot and Tafel slope analysis plot from the 5-mV s^{-1} scan rate plot. F) CV data and the forward-scan convoluted potential sweep voltammetry data for the same CV data.

The y-intercept of Eq. (2) can be represented as follows:

$$Y = E^{o'} + \frac{RT}{(1-\alpha)n_\alpha F} \times \{0.78 + \frac{2.3}{2}\log\left[\frac{(1-\alpha)n_\alpha FD}{k^2RT}\right] \quad (3)$$

Where $E^{o'}$ denotes the underlying standard electrode potential corresponding to BPA oxidation and can be derived from a Tafel plot; *k* is the heterogeneous rate constant relating to the electron-transfer process; and *D* is the diffusion coefficient.

Later, we estimated the related electro-effective surface area (*A*) of the electrode by using the slope of the following equation:

$$I_p = 2.99 \times 10^5 n[(1-\alpha)n_\alpha]^{1/2} C_o A D^{1/2} v^{1/2} \quad (4)$$

Where C_o is the bulk concentration of the BPA solution. We found that the value was approximately 1.31 cm^2 when the bulk concentration was 0.5 μM. For PANI/GCE, a 5 μM BPA solution was used and $A = 0.63$ cm^2. The lower *A* value is in agreement with our CV and DPV results, in which PANI/GCE produced a lower current signal compared to the PANI_AuNPs/GCE for the same 50 μM BPA solution. Hence, even though the transition relating to the RDS is more product-like for PANI/GCE, its *A* value is only about half the value determined for PANI_AuNPs/GCE.

Next, we evaluated the experimental Tafel plot for the aforementioned electrochemical process over the electrode system. Generally, Tafel slope analysis allows the evaluation of one or more linear regions, which can be used to determine the number of electrons (n) transferred while making a paradigm shift from transition state to the product in the RDS [25]. Fig. 6E shows the experimental plot for both oxidation and reduction waves at a scan rate of 5 mV s^{-1}. The Tafel plot for PANI/GCE is shown in Figure S8E. Both figures clearly show linear regions, also known as the Tafel region, which is expressed by the following regression equation:

$$\log I = 2.3 + (-25.19)\eta \quad (5)$$

The value of n can be evaluated by using the following slope equation:

$$\frac{1}{b} = \frac{n\alpha F}{2.303RT} \quad (6)$$

Where *b* denotes the Tafel slope, which is calculated as 39.7 mV dec^{-1} and 117.65 mV dec^{-1} for the PANI_AuNPs/GCE and PANI/GCE, respectively. Solving this equation yields an *n* value of about 2, which indicates that the oxidation of BPA involves the transfer of two electrons at the interface region. Furthermore, the value of $E^{o'}$ was calculated to be 0.45 V.

To determine the corresponding diffusion coefficient (*D*) for the BPA oxidation process, we investigated the convoluted potential sweep voltammetry (CPSV) plot at 5 mV s^{-1} (Fig. 6F). The CPSV is a sigmoidal-shaped curve, which is beneficial for resolving kinetic parameters over direct B–V theory [36]. The CPSV plot typically forms a current plateau over positive potential, demonstrating a limiting current level. The limiting current (I_l) can be expressed as follows [36]:

$$I_l = nFAC_o\sqrt{D} \quad (7)$$

The value of *D* was estimated to be about 5.83×10^{-6} cm^2 s^{-1}, which is almost identical to the previously reported value [37]. By using Eq. (2), the *k* values were determined to be approximately 7.02×10^{-4} cm s^{-1} and 1.18×10^{-4} cm s^{-1} for PANI_AuNPs/GCE and PANI/GCE, respectively.

Solution pH variation analysis was carried out to understand the effect of proton concentration on the oxidation of BPA at the PANI_AuNPs/GCE. Fig. 7A shows CVs for solutions with pH in the range of 4 to 9. With varying pH, both the peak potential and peak current changed for the BPA solutions, making it clear that BPA oxidation at the PANI_AuNPs/GCE is dependent on proton concentration. Fig. 7B shows the peak current density (red plot) vs. supporting electrolyte pH plot. The plot shows the highest current densities around the neutral pH region (pH 6.0 and 7.0). BPA has a *pKa* value of 9.3 [14]. Therefore, below pH 9.0, BPA primarily exists in its neutral form and in its anionic phenolate form above this value. With increasing pH, the proton pressure of the solution decreases. Fig. 7B also shows that with increasing pH, the peak potentials shift towards the negative. Hence, less energy is required for BPA oxidation with decreasing proton pressure. Therefore, it is likely

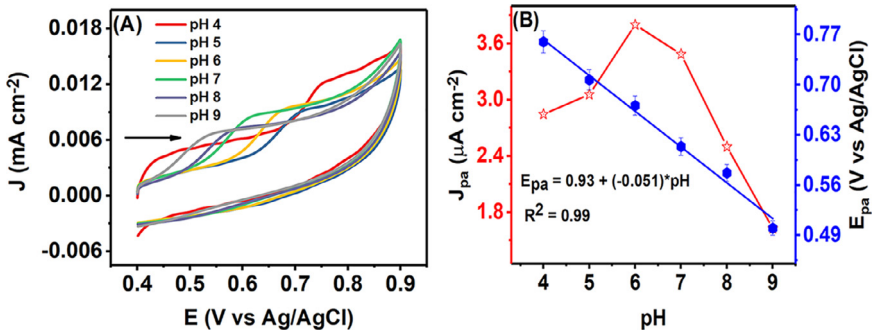

Fig. 7. Solution pH effect on the oxidation of BPA at the PANI_AuNPs/GCE interface. A) CV measurements in 0.1 M PBS solutions with varying pH (4 – 9) containing 10 μM BPA. B) Plot of peak current densities (red) and peak potentials (blue) at different pH solutions. (For interpretation of the references to colour in this figure legend, the reader is referred to the web version of this article.)

that this decreased proton pressure is responsible for the higher current value observed for pH 6.0 and pH 7.0. These results indicate that oxidation of BPA is accompanied by deprotonation [8,13]. However, in basic solutions, the peak current density decreases, which may be due to the presence of the phenolate form of BPA [14]. This anionic form might have hindered the approach of BPA at the electrode surface and resulted in the decreased peak current density. The relationship between proton and electron transfer can be determined from the following equation:

$$E_p = E^o + \frac{0.059}{n}\log\left\{\frac{(Ox)^o}{(Red)^r}\right\} - \frac{0.059m}{n}pH \quad (8)$$

Here, Ep = peak potential, $E°$ = formal potential, m = number of proton transfer, and n = number of electron transfer. Therefore, from the slope of peak potential vs. pH, m/n can be determined. The slope of 0.051 is close to the theoretical value of 1:1 proton and electron transfer [38]. We observed in the Tafel slope analysis that overall $2e^-$ transfer took place during BPA oxidation. Thus, the BPA oxidation followed a $2e^-/2H^+$ transfer process.

Solving Eq. (9) for the values $n_b = 1$, $n_r = 1$, $v = 1$, and $\beta = 0.31$ and substituting the value of α_a into Eq. (6) further confirmed that the oxidation of BPA followed at least two-electron transfer steps, and the RDS is the second electron transfer step for the PANI_AuNPs/GCE. Again, taking $n_b = 0$, $n_r = 1$, $v = 1$, and $\beta = 0.25$ for PANI/GCE, we obtained a b value of 118.27 mV dec^{-1} from Eq. (6). This indicates that at the PANI/GCE interface, the RDS for BPA oxidation is the first electron-transfer step. This result is analogous to our experimental findings. Previous kinetic analyses on water oxidation have shown that the first electron-transfer RDS is kinetically less favorable then a second electron-transfer RDS [39].

An analysis of pH variation indicated that the BPA oxidation process is dependent on the proton concentration of the solution. Eq. (8) shows that the number of the proton (H^+) transfer was also two. Based on these analyses, we can conclude that in the PANI_AuNPs/GCE system, the BPA is oxidized by losing two protons from its hydroxyphenyl groups. However, it is unlikely that the process included any chemical step between the electron transfer steps and the oxidation reaction:

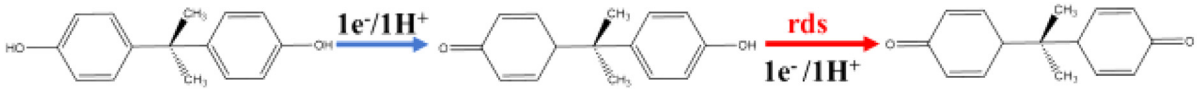

3.4. Possible oxidation mechanism of BPA at the PANI_AuNPs/GCE interface

In the previous section, we discussed the kinetics of BPA oxidation at the PANI_AuNPs/GCE and PANI/GCE surfaces. The scan rate variation analysis revealed that the oxidation process is diffusion controlled. Hence, between diffusion and adsorption of the analyte at the interfacial region, diffusion is the slower step. We determined the value of D to be 5.83×10^{-6} cm^2 s^{-1} from Eq. (7). Scheme 2A shows the diffusion of the BPA from bulk to the PANI_AuNPs/GCE interface. The slow diffusion coefficient of BPA indicates that electron transfer occurred quickly once the analyte reached the PANI_AuNPs interface at the inner Helmholtz plane (IHP). Scan rate analysis also revealed that the BPA oxidation process is irreversible from the plot of I_pC^{-1} $v^{-1/2}$ against log v. Then again, the Tafel plot analysis revealed that the oxidation followed a two-electron ($2e^-$) transfer process with a slope of ≈39.7 mV dec^{-1} and 117.65 mV dec^{-1} for PANI_AuNPs/GCE and PANI/GCE, respectively. This is a multistep electron-transfer process, so we used the Bockris and Reddy equation for determining the consecutive steps that took place during BPA oxidation [39]:

$$\alpha_a = \frac{n_b}{v} + n_r\beta \quad (9)$$

Here, α_a is the multi-step electron transfer coefficient, n_b is the electron transfer that took place before the RDS, v is the number of RDSs in the overall electrochemical reaction, n_r is the number of electrons transferred during the RDS, and β is the symmetry factor.

However, the kinetic analysis alone is not sufficient to understand the electrocatalytic ability of PANI_AuNPs towards BPA oxidation at the PANI_AuNPs/GCE system because it does not give any molecular information. For this, we need to consider the physical and electrochemical properties of the PANI_AuNPs composite. FE-SEM analysis revealed that the ultrasonication method distributed AuNPs throughout the PANI surface. Then, from EDS characterization of the PANI_AuNPs composite, we saw that aside from C and Au, it is also rich in N and O elements. XPS characterization revealed that PANI contained partial negative charge bearing functional groups such as –OH, –COOH, and –NH. These groups, along with the AuNPs on the surface, may have provided the interfacial region for the interaction of BPA with PANI_AuNPs for the electron-transfer process. It is likely that the BPA approached the PANI_AuNPs surface and interacted through electrostatic forces with the AuNPs and functional groups [29].

Hydrogen bonding may have also been part of the interaction process [23,30], as shown in Scheme 2B. The pH variation results support this hypothesis. The AuNPs likely interacted with the oxygen groups of BPA, while the partial negative charge bearing functional groups of PANI interacted through the hydrogen atoms. This then led to the first electron transfer at the lower positive potential compared to the bare GCE. The process is shown in Scheme 2C. After the first electron transfer, the partially oxidized BPA molecules required reorientation for the second electron transfer to take place. Analysis of the Tafel plot showed that the second electron-transfer process was the RDS. However, this was still faster than the diffusion coefficient, as the k value was found to

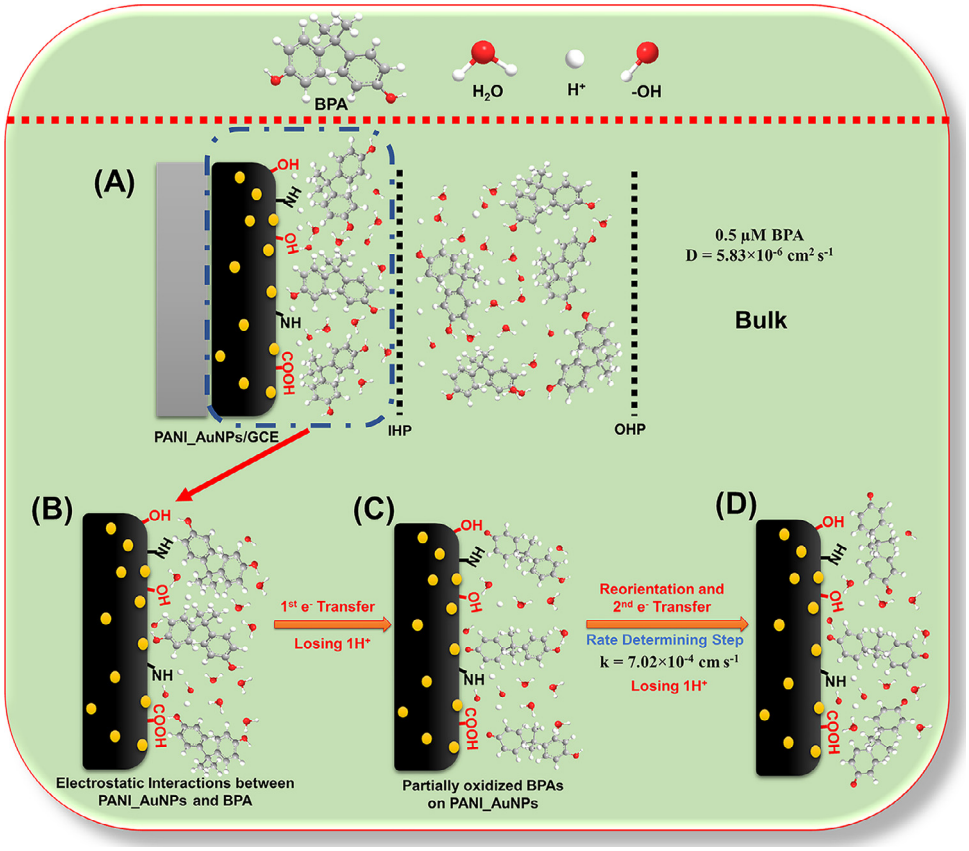

Scheme 2. The possible oxidation mechanism for BPA at the PANI_AuNPs/GCE. A) Diffusion of BPA molecules from the bulk to the inner Helmholtz plane (IHP) and interaction with the PANI_AuNPs/GCE interface. B) Possible orientation of BPA molecules while interacting with the PANI_AuNPs surface. C) After transferring one electron, the partially oxidized BPA molecules at the interface of PANI_AuNPs. D) BPA molecules after the second electron transfer and complete oxidation at the PANI_AuNPs surface.

be 7.02 × 10^{-4} cm s^{-1}, which is significantly higher than that for the PANI/GCE system. After complete oxidation, the BPA molecules likely moved away from the PANI_AuNPs surface. This process is shown in Scheme 2D.

These results indicate that the PANI and AuNPs worked synergistically during BPA oxidation. As a result, the electrocatalyst provided an increased surface area that allowed for a higher quantity of BPA molecules to be oxidized. At the same time, the PANI_AuNPs interacted with the BPA molecules to provide a lower activation energy pathway for oxidation. The α value of 0.69 also confirmed this analysis, suggesting that conducting polymers that contain various functionalities can be combined with metal nanoparticles though ultrasonication to prepare highly effective BPA electrocatalysts.

3.5. Quantitative detection of BPA at PANI_AuNPs/GCE interface

We used the DPV technique for the quantitative detection of BPA in various concentrations, as it is one of the common pulse techniques that can be used for sensitive detection of analytes. Fig. 8A shows the DPV plots for BPA in the concentration of 3 × 10^{-9} M (0.003 µM) to 45.69 × 10^{-6} M (45.69 µM) in neutral pH PBS (0.1 M). The concentration variation plots show that the current signal increased with each addition of BPA. However, at higher BPA concentrations, the peak potentials started to shift towards more positive potentials. This might be due to the fouling of the PANI_AuNPs/GCE surface.

Peak current densities plotted against the concentrations of BPA gave two linear fits (Figs. 8B and 8C). The first linear fit was from 0.003 to 0.064 µM, and the second linear fit was in the range of 0.075 to 45.69 µM. The obtained regression equations for the two linear fits were J_{pa} (A cm^{-2}) = −2.59 × 10^{-10} (A cm^{-2}) + 1.76 × 10^{-6} (A cm^{-2} μM^{-1}) × [BPA] (µM) and J_{pa} (A cm^{-2}) = 1.64 × 10^{-7} (A cm^{-2}) + 2.68 × 10^{-8} (A cm^{-2} μM^{-1}) × [BPA] (µM). These equations show that the sensitivity for the 0.003–0.064 µM range was 1.76 µA cm^{-2} μM^{-1}, and for the 0.075–45.69 µM range it was only 0.027 µA cm^{-2} μM^{-1}. This result confirmed that at higher concentrations of BPA the electrode has lower sensitivity. The LOD was determined to be 0.0004 µM (0.4 nM) using the formula LOD = 3.3 × SD/S, where SD = standard error and S = slope. The high sensitivity and low LOD value suggest that the PANI_AuNPs/GCE is a highly effective BPA sensor. The performance of the PANI_AuNPs/GCE is compared with other BPA sensors in Table 1. A comparison of the data shows that the proposed PANI_AuNPs/GCE has a lower LOD and wider linear range compared to many of the reported electrochemical BPA sensors.

3.6. Testing the selectivity of the PANI_AuNPs/GCE toward BPA

It is important that the sensor avoids interference from unwanted chemical species so that it can give an accurate quantitative result of BPA. Therefore, we tested its response to other chemicals that are usually present with BPA in the environment [17]. We used 0.1 M PBS of 0.1 (pH 7.0) and the DPV technique to analyze a 1 µM solution of BPA. The red curve in Fig. 9 shows that there was a clear response from the electrode for the BPA solution. To test the interfering species, we used at least a 500 times higher concentration; concentrations of HQ, phenol, 4-nitrophenol (4-NP), and CT were 0.5 mM or 500 µM, and $NaCO_3$ and NH_4Cl were tested in 1 mM concentrations. The rest of the interfering chemicals were present in a concentration of 10 mM. As shown in Fig. 9, there

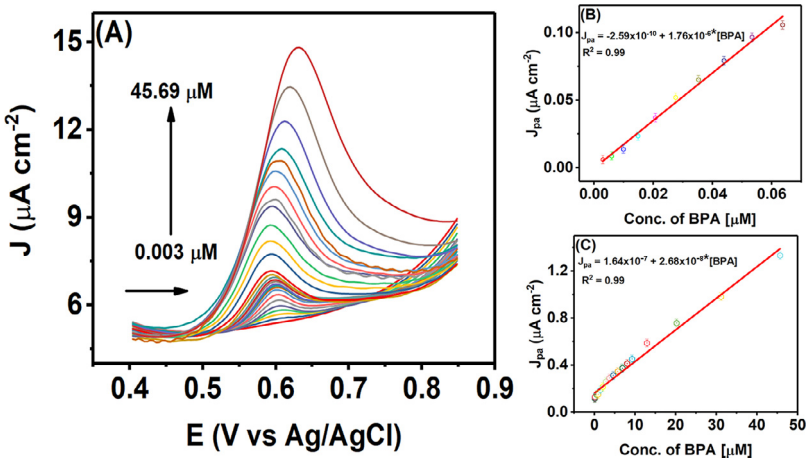

Fig. 8. DPV plots of various concentrations of BPA in 0.1 M PBS (pH 7.0) supporting electrolyte solution and their corresponding calibration plots. A) The following BPA concentrations were utilized for the concentration variation analysis: 0.003, 0.06, 0.01, 0.015, 0.02, 0.028, 0.035, 0.044, 0.053, 0.064, 0.075, 0.087, 0.1, 0.11, 0.52, 0.91, 1.43, 2.06, 2.81, 3.67, 4.64, 5.74, 6.89, 8.05, 9.26, 12.92, 20.22, 31.16, and 45.69 µM. B,C) Peak current density (J_{pa}) vs. concentration plots with linear fitting equations.

Table 1
Comparing the linear range, sensitivity, and LOD of the PANI_AuNPs/GCE for BPA oxidation with previously reported sensors.

Modified Electrode	Technique	Linear Range (µM)	Detection Limit (µM)	Sensitivity(µA cm^{-2} $µM^{-1}$)	Reference
XOD/GCE	amperometry	0.001–0.041	0.001	0.025	[7]
PANI/MWCNT/PGE	amperometry	1 – 400	0.01	–	[8]
AuNPs/SGNF/GCE	LSV	0.08–250	0.035	–	[11]
AuNPs/PVP/PGE	SWAdSV	0.023–1.10	0.001	–	[12]
Rh_2O_3–rGO/GCE	CV	0.6 – 40	0.12	–	[13]
Cu_Zn/GO/GCE	SWV	0.003–20	0.00088	–	[14]
Ru/PANI/g-C_3N_4	DPV	0.01–1.1	0.00018	1.6	[17]
PANI-GO/GCE	DPV	0.002–0.1 0.1 – 3	0.0005	–	[18]
AuNPs/CBNPs/SPCE	DPV	0.01–10	0.0003	–	[19]
NiNP/NCN/CS/GCE	DPV	0.1 – 2.5 2.5 – 15	0.045	–	[40]
MWCNTs-PDDA-AuPd/GCE	DPV	0.18–18	0.006	–	[41]
PANI_AuNPs/GCE	DPV	0.003–0.064 0.075–45.69	0.0004	1.76 0.027	This Work

XOD: xanthine oxidase; MWCNT: multi-walled carbon nanotube; PGE: pencil graphite electrode; SGNF: stacked graphene nanofibers; PVP: polyvinylpyrrolidone; rGO: reduced graphene oxide; CBNPs: carbon black nanoparticles; NCN: nitrogen-doped carbon nanosheet; PDDA: poly(diallyldimethylammonium chloride).

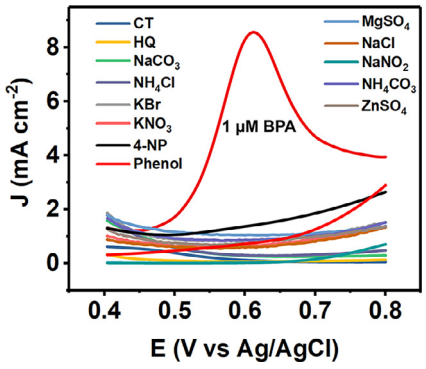

Fig. 9. Testing the selectivity of PANI_AuNPs/GCE sensor in the presence of interfering species. DPV plots showing the response of PANI_AuNPs/GCE in the presence of BPA, CT, HQ, $NaCO_3$, NH_4Cl, KBr, KNO_3, $MgSO_4$, NaCl, $NaNO_2$, NH_4CO_3, $ZnSO_4$, 4-NP, and phenol.

were slight changes in the charging current for different interfering species. None of them showed any detectable signal in the potential window of BPA oxidation, whereas 1 µM BPA gave a clear response. This analysis demonstrates that the PANI_AuNPs/GCE can detect BPA with excellent selectivity, even in the presence of interfering species in extremely high concentrations.

3.7. Stability and reproducibility of BPA oxidation at PANI_AuNPs/GCE interface

We tested the experimental stability of the PANI_AuNPs/GCE with DPV experiments. Fig. 10A shows 45 consecutive DPV plots taken in BPA solution. The data shows very little change with respect to consecutive DPV runs. The small RSD value of 3.49% shows that the PANI_AuNPs/GCE system is very stable in 1 µM BPA solution. The modified electrodes were stored for 28 days at RT for checking the storage stability. The peak current signal decreased by 4.31% at the 28th day compared to the newly modified electrode.

We tested the reproducibility of the PANI_AuNPs/GCE by modifying four different GCEs with PANI_AuNPs. DPV plots of 1 µM BPA in 0.1 M neutral PBS were recorded, and the peak current values are shown in Fig. 10B. The four electrodes showed almost similar peak current values. Both the stability and reproducibility tests confirm that the PANI_AuNPs/GCE is suitable for practical purposes.

3.8. Detecting BPA in water samples and beverage with PANI_AuNPs/GCE

In order to test the effectiveness of the PANI_AuNPs/GCE sensor for practical applications, we used tap water, water from plastic bottles, and canned beverages. The tap water was used as is

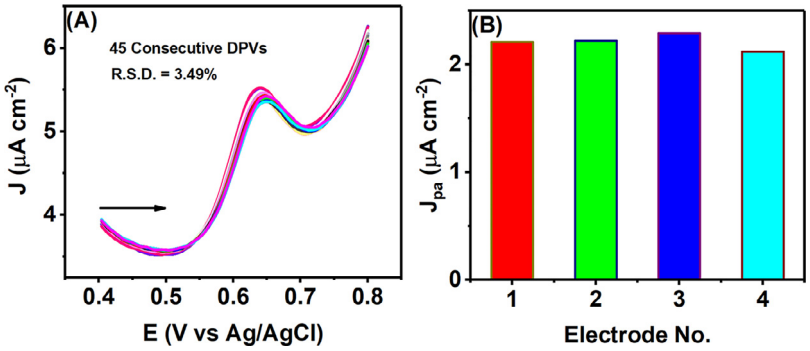

Fig. 10. Stability and experimental reproducibility data. A) 45 consecutive DPV plots taken for 1 μM BPA in 0.1 M neutral PBS. B) Peak current density values for four different electrodes taken in a solution of 1 μM BPA in 0.1 M neutral PBS.

Table 2
BPA detection test using PANI_AuNPs/GCE sensor with tap water, bottled water, and canned beverage.

Tap Water Sample no.	BPA added (μM)	BPA found (μM)[a]	RSD (%)	Recovery (%)
1	0.5	0.51	1.40	102
2	0.75	0.73	1.91	97.33
3	1	0.99	0.71	99
4	5	4.96	0.57	99.2
Bottled Water Sample no.	**BPA added (μM)**	**BPA found (μM)[a]**	**RSD (%)**	**Recovery (%)**
1	0.5	0.49	2.89	98
2	0.75	0.74	0.94	98.67
3	1	1.03	1.40	103
4	5	5.23	3.18	104.6
Beverage Sample no.	**BPA added (μM)**	**BPA found (μM)[a]**	**RSD (%)**	**Recovery (%)**
1	0.5	0.52	2.77	104
2	0.75	0.77	1.86	102.67
3	1	1.02	1.40	102
4	5	5.19	2.64	103.8

[a] Average of four tests.

because it contains various ionic species that might interfere with BPA sensing [42]. For these tests, we spiked the samples with 0.5, 0.75, 1, and 5 μM BPA. Each sample was tested four times, and the average of the results is reported in Table 2. The results show that the PANI_AuNPs/GCE sensor performs very well in detecting BPA in real samples.

Conclusion

We reported a highly sensitive BPA sensor in which PANI and AuNPs composites were utilized as the electrode material. Two synthetic pathways were followed to prepare the composites. Firstly, PANI was prepared via chemical initiation followed by termination with distilled water. Secondly, the PANI_AuNPs composite was synthesized via an ultrasonication method. The composite material retained the crystalline Au structure, as confirmed through XRD analysis. The crystalline nature of AuNPs likely increased the conductivity of the composite to facilitate the oxidation of BPA. We also studied the oxidation kinetics through CV, CPSV, and Tafel plot analysis. These studies demonstrated that the oxidation of BPA is a two-electron-transfer process. Furthermore, the oxidation occurred through a multistep reaction process in which the second step was likely the RDS. To understand the mechanism beyond the kinetic evaluation, we further analyzed how the composite interacted with the BPA molecule. It is likely that the surface functional groups of PANI and AuNPs actively participated in electrostatic interactions with the BPA. Finally, both PANI and AuNPs in the composite assisted in the successful anchoring of BPA over the electrode surface and consecutive facile electron transfer. The electrode showed two linear ranges from the nanomolar to micromolar region (0.003–0.064 μM and 0.075–45.69 μM), with an LOD as low as 0.4 nM. We further utilized the sensor to detect BPA in tap water, bottled water, and canned beverage, which confirmed its effectiveness in real-time analysis.

Declaration of Competing Interest

The authors declare that they have no known competing financial interests or personal relationships that could have appeared to influence the work reported in this paper.

Credit authorship contribution statement

Md. Mahedi Hasan: Conceptualization, Investigation, Writing – original draft. **Tamanna Islam:** Conceptualization, Investigation, Writing – original draft. **Al Imran:** Investigation. **Bassam Alqahtani:** Writing – review & editing. **Syed Shaheen Shah:** Formal

analysis, Writing – review & editing. **Wael Mahfoz:** Investigation. **Mohammad Rezaul Karim:** Funding acquisition, Writing – review & editing. **Hamad F. Alharbi:** Writing – review & editing. **Md. Abdul Aziz:** Conceptualization, Supervision. **A.J. Saleh Ahammad:** Conceptualization, Supervision.

Acknowledgements

This work was supported by the Ministry of Education, Bangladesh (Project ID: PS20191122). The authors extend their appreciation to the Deanship of Scientific Research at King Saud University for funding this work through research group no (RG- 1440-102). The authors also acknowledge the support from the Center of Excellence in Nanotechnology (CENT), King Fahd University of Petroleum & Minerals, Saudi Arabia.

Supplementary materials

Supplementary material associated with this article can be found, in the online version, at doi:10.1016/j.electacta.2021.137968.

References

[1] S.A. Vogel, The politics of plastics: the making and unmaking of bisphenol a "safety", Am. J. Public Health. 99 (2009) 559–566, doi:10.2105/ajph.2008.159228.
[2] K. Sharif, B. Lichtbroun, C. Rizenbah, Y. Shoenfeld, The Role of Plastics in the Spectrum of Autoimmune Disease-Bisphenol A, Elsevier Inc., 2019, doi:10.1016/B978-0-12-814307-0.00039-6.
[3] A. George, E. Thomas, W. Rolf, Polycarbonates in: ullmann's, Encycl. Ind. Chem. (2014) 1–17, doi:10.1002/14356007.a21_207.pub2.
[4] P. Czub, Synthesis of high-molecular-weight epoxy resins from modified natural oils and Bisphenol A or Bisphenol A-based epoxy resins, Polym. Adv. Technol. 20 (2009) 194–208, doi:10.1002/pat.1252.
[5] D.J. Plazek, I.C. Choy, The physical properties of bisphenol-a-based epoxy resins during and after curing. II. Creep behavior above and below the glass transition temperature, J. Polym. Sci. Part B Polym. Phys. 27 (1989) 307–324, doi:10.1002/polb.1989.090270207.
[6] A. Shafei, M. Matbouly, E. Mostafa, S. Al Sannat, M. Abdelrahman, B. Lewis, B. Muhammad, S. Mohamed, R.M. Mostafa, Stop eating plastic, molecular signaling of bisphenol A in breast cancer, Environ. Sci. Pollut. Res. 25 (2018) 23624–23630, doi:10.1007/s11356-018-2540-y.
[7] N. Ben Messaoud, M.E. Ghica, C. Dridi, M. Ben Ali, C.M.A. Brett, A novel amperometric enzyme inhibition biosensor based on xanthine oxidase immobilised onto glassy carbon electrodes for bisphenol A determination, Talanta 184 (2018) 388–393, doi:10.1016/j.talanta.2018.03.031.
[8] S. Poorahong, C. Thammakhet, P. Thavarungkul, W. Limbut, A. Numnuam, P. Kanatharana, Amperometric sensor for detection of bisphenol A using a pencil graphite electrode modified with polyaniline nanorods and multiwalled carbon nanotubes, Microchim. Acta 176 (2012) 91–99, doi:10.1007/s00604-011-0698-9.
[9] Z. Lin, L. Wang, Y. Jia, Y. Zhang, Q. Dong, C. Huang, A study on environmental bisphenol a pollution in plastics industry areas, Water. Air. Soil Pollut. 228 (2017), doi:10.1007/s11270-017-3277-9.
[10] T. Yamamoto, A. Yasuhara, Quantities of bisphenol A leached from plastic waste samples, Chemosphere 38 (1999) 2569–2576, doi:10.1016/S0045-6535(98)00464-0.
[11] X. Niu, W. Yang, G. Wang, J. Ren, H. Guo, J. Gao, A novel electrochemical sensor of bisphenol A based on stacked graphene nanofibers/gold nanoparticles composite modified glassy carbon electrode, Electrochim. Acta 98 (2013) 167–175, doi:10.1016/j.electacta.2013.03.064.
[12] Y.T. Yaman, S. Abaci, Sensitive adsorptive voltammetric method for determination of Bisphenol A by gold nanoparticle/polyvinylpyrrolidone-modified pencil graphite electrode, Sensors (Switzerland) 16 (2016), doi:10.3390/s16060756.
[13] R. Shi, X. Yuan, A. Liu, M. Xu, Z. Zhao, Determination of bisphenol a in beverages by an electrochemical sensor based on Rh_2O_3/reduced graphene oxide composites, Appl. Sci. 8 (2018), doi:10.3390/app8122535.
[14] Ş.Ulubay Karabiberoğlu, Sensitive voltammetric determination of bisphenol a based on a glassy carbon electrode modified with copper oxide-zinc oxide decorated on graphene oxide, Electroanalysis 31 (2019) 91–102, doi:10.1002/elan.201800415.
[15] A.J.S. Ahammad, T. Islam, M.M. Hasan, Graphene-based electrochemical sensors for biomedical applications, in: Biomedical Applications of Graphene and 2D Nanomaterials, Elsevier Inc., 2019, pp. 249–282, doi:10.1016/b978-0-12-815889-0.00012-x.
[16] T. Islam, M.M. Hasan, S.S. Akter, N.H. Alharthi, M.R. Karim, M.A. Aziz, M.D. Hossain, A.J.S. Ahammad, Fabrication of Ni–Co-based heterometallo-supramolecular polymer films and the study of electron transfer kinetics for the nonenzymatic electrochemical detection of nitrite, ACS Appl. Polym. Mater. 2 (2020) 273–284, doi:10.1021/acsapm.9b00797.
[17] S.K. Ponnaiah, P. Prakash, S. Muthupandian, Ultrasonic energy-assisted in-situ synthesis of Ru0/PANI/g-C3N4 nanocomposite: application for picomolar-level electrochemical detection of endocrine disruptor (Bisphenol-A) in humans and animals, Ultrason. Sonochem. (2019) 58, doi:10.1016/j.ultsonch.2019.104629.
[18] G. Zhu, Q. Tang, J. Dou, X. Li, J. Yang, R. Xu, J. Liu, Partially reduced graphene oxide sheet-covered polyaniline nanotubes for the simultaneous determination of Bisphenol A and Phenol, J. Electrochem. Soc. 166 (2019) B1661–B1668, doi:10.1149/2.1381915jes.
[19] N. Ben Messaoud, A. Ait Lahcen, C. Dridi, A. Amine, Ultrasound assisted magnetic imprinted polymer combined sensor based on carbon black and gold nanoparticles for selective and sensitive electrochemical detection of Bisphenol A, Sens. Actuat. B Chem. 276 (2018) 304–312, doi:10.1016/j.snb.2018.08.092.
[20] J. Zou, G.Q. Zhao, J. Teng, Q. Liu, X.Y. Jiang, F.P. Jiao, J.G. Yu, Highly sensitive detection of bisphenol A in real water samples based on in-situ assembled graphene nanoplatelets and gold nanoparticles composite, Microchem. J. 145 (2019) 693–702, doi:10.1016/j.microc.2018.11.040.
[21] L. Hu, C.C. Fong, X. Zhang, L.L. Chan, P.K.S. Lam, P.K. Chu, K.Y. Wong, M. Yang, Au nanoparticles decorated TiO_2 nanotube arrays as a recyclable sensor for photoenhanced electrochemical detection of bisphenol A, Environ. Sci. Technol. 50 (2016) 4430–4438, doi:10.1021/acs.est.5b05857.
[22] M. Dietrich, M. Franke, M. Stelter, P. Braeutigam, Degradation of endocrine disruptor bisphenol A by ultrasound-assisted electrochemical oxidation in water, Ultrason. Sonochem. 39 (2017) 741–749, doi:10.1016/j.ultsonch.2017.05.038.
[23] M.M. Hasan, T. Islam, S.S. Akter, N.H. Alharthi, M.R. Karim, M.A. Aziz, A. Awal, M.D. Hossain, A.J.S. Ahammad, Computational approach to understanding the electrocatalytic reaction mechanism for the process of electrochemical oxidation of nitrite at a Ni–Co-based heterometallo-supramolecular polymer, ACS Omega 5 (2020) 12882–12891, doi:10.1021/acsomega.0c00658.
[24] A.J.S. Ahammad, M.K. Alam, T. Islam, M.M. Hasan, R. Karim, A.N. Anju, M.N.I. Mozumder, Poly (brilliant cresyl blue)-reduced graphene oxide modified activated GCE for nitrite detection: analyzing the synergistic interactions through experimental and computational study, Electrochim. Acta 349 (2020) 136375, doi:10.1016/j.electacta.2020.136375.
[25] K.S. Exner, H. Over, Beyond the rate-determining step in the oxygen evolution reaction over a single-crystalline IrO2(110) model electrode: kinetic scaling relations, ACS Catal. 9 (2019) 6755–6765, doi:10.1021/acscatal.9b01564.
[26] N.Y. Abu-Thabit, Chemical oxidative polymerization of polyaniline: a practical approach for preparation of smart conductive textiles, J. Chem. Educ. 93 (2016) 1606–1611, doi:10.1021/acs.jchemed.6b00060.
[27] X. Hu, N. Takada, S. Machmudah, Wahyudiono, H. Kanda, M. Goto, Ultrasonic-enhanced fabrication of metal nanoparticles by laser ablation in liquid, Ind. Eng. Chem. Res. 59 (2020) 7512–7519, doi:10.1021/acs.iecr.9b06384.
[28] A.J.S. Ahammad, M.M. Hasan, T. Islam, M.O. Al-Shehri, A.N. Anju, M.K. Alam, J.P. Kim, M.A.A. Qasem, M.A. Aziz, Pyrolytic preparation of gold nanoparticle-coated taro carbon and its application for the selective detection of dopamine, New J. Chem. 42 (2018) 4543–4552, doi:10.1039/c7nj04777k.
[29] A.J.S. Ahammad, N. Odhikari, S.S. Shah, M.M. Hasan, T. Islam, P.R. Pal, M.A. Ahmed Qasem, M.A. Aziz, Porous tal palm carbon nanosheets: preparation, characterization and application for the simultaneous determination of dopamine and uric acid, Nanoscale Adv. 1 (2019) 613–626, doi:10.1039/c8na00090e.
[30] T. Islam, M.M. Hasan, S.S. Shah, M.R. Karim, F.S. Al-Mubaddel, M.H. Zahir, M.A. Dar, M.D. Hossain, M.A. Aziz, A.J.S. Ahammad, High yield activated porous coal carbon nanosheets from Boropukuria coal mine as supercapacitor material: investigation of the charge storing mechanism at the interfacial region, J. Energy Storage 32 (2020) 101908, doi:10.1016/j.est.2020.101908.
[31] H. Hu, X.J. Hou, X.C. Wang, J.J. Nie, Q. Cai, F.J. Xu, Gold nanoparticle-conjugated heterogeneous polymer brush-wrapped cellulose nanocrystals prepared by combining different controllable polymerization techniques for theranostic applications, Polym. Chem. 7 (2016) 3107–3116, doi:10.1039/c6py00251j.
[32] M.R. Bindhu, M. Umadevi, Silver and gold nanoparticles for sensor and antibacterial applications, Spectrochim. Acta - Part A Mol. Biomol. Spectrosc. 128 (2014) 37–45, doi:10.1016/j.saa.2014.02.119.
[33] S. Pruneanu, E. Veress, I. Marian, L. Oniciu, Characterization of polyaniline by cyclic voltammetry and UV-Vis absorption spectroscopy, J. Mater. Sci. 34 (1999) 2733–2739, doi:10.1023/A:1004641908718.
[34] N. Shoaie, M. Forouzandeh, K. Omidfar, Voltammetric determination of the Escherichia coli DNA using a screen-printed carbon electrode modified with polyaniline and gold nanoparticles, Microchim. Acta 185 (2018) 1–9, doi:10.1007/s00604-018-2749-y.
[35] G. Zhao, G. Liu, Electrochemical deposition of gold nanoparticles on reduced graphene oxide by fast scan cyclic voltammetry for the sensitive determination of As(III), Nanomaterials 9 (2019) 1–13, doi:10.3390/nano9010041.
[36] M.A. Hasnat, M.M. Hasan, N. Tanjila, M.M. Alam, M.M. Rahman, pH dependent kinetic insights of electrocatalytic arsenite oxidation reactions at Pt surface, Electrochim. Acta 225 (2017) 105–113, doi:10.1016/j.electacta.2016.12.055.
[37] K.A. Schult, D.R. Paul, Water Sorption and Transport in a Series of Polysulfones, J. Polym. Sci. Part A Polym. Chem. (1996) 2804–2817.
[38] M.A. Haque, M.M. Hasan, T. Islam, M.A. Razzak, N.H. Alharthi, A. Sindan, M.R. Karim, S.I. Basha, M.A. Aziz, A.J.S. Ahammad, Hollow reticular shaped highly ordered rice husk carbon for the simultaneous determination of dopamine and uric acid, Electroanalysis (2020) 1–15, doi:10.1002/elan.202060059.

[39] N.T. Suen, S.F. Hung, Q. Quan, N. Zhang, Y.J. Xu, H.M. Chen, Electrocatalysis for the oxygen evolution reaction: recent development and future perspectives, Chem. Soc. Rev. 46 (2017) 337–365, doi:10.1039/c6cs00328a.
[40] Y. Wang, C. Yin, Q. Zhuang, An electrochemical sensor modified with nickel nanoparticle/nitrogen-doped carbon nanosheet nanocomposite for bisphenol A detection, J. Alloys Compd. 827 (2020) 154335, doi:10.1016/j.jallcom.2020.154335.
[41] F. Mo, J. Xie, T. Wu, M. Liu, Y. Zhang, S. Yao, A sensitive electrochemical sensor for bisphenol A on the basis of the AuPd incorporated carboxylic multi-walled carbon nanotubes, Food Chem. 292 (2019) 253–259, doi:10.1016/j.foodchem.2019.04.034.
[42] M.S. Nahar, J. Zhang, A. Ueda, F. Yoshihisa, Investigation of severe water problem in urban areas of a developing country: the case of Dhaka, Bangladesh, Environ. Geochem. Health 36 (2014) 1079–1094, doi:10.1007/s10653-014-9616-5.